EVALUATION OF AIRFOIL DYNAMIC STALL CHARACTERISTICS FOR MANEUVERABILITY

William G. Bousman

Army/NASA Rotorcraft Division
Aeroflightdynamics Directorate (AMRDEC)
US Army Aviation and Missile Command
Ames Research Center, Moffett Field, California

Abstract

The loading of an airfoil during dynamic stall is examined in terms of the augmented lift and the associated penalties in pitching moment and drag. It is shown that once stall occurs and a leading-edge vortex is shed from the airfoil there is a unique relationship between the augmented lift, the negative pitching moment, and the increase in drag. This relationship, referred to here as the dynamic stall function, shows limited sensitivity to many parameters that influence rotors in flight. For single-element airfoils it appears that there is little that can be done to improve rotorcraft maneuverability except to provide good static $c_{l_{max}}$ characteristics and the chord or blade number that is required to provide the necessary rotor thrust. The loading on a helicopter blade during a severe maneuver is examined and it is shown that the blade's dynamic stall function is similar to that obtained in two-dimensional wind tunnel testing. An evaluation of three-dimensional effects for flight and an oscillating wing in a wind tunnel suggests that the two problems are not proper analogues. The utility of the dynamic stall function is demonstrated by evaluating sample theoretical predictions based on semi-empirical stall models and CFD computations. The approach is also shown to be useful in evaluating multi-element airfoil data obtained from dynamic stall tests.

1 Nomenclature

a_i, b_i	polynomial coefficients for $c_{l_{max}}$, $i = 0,1,2$
c	blade chord, ft
c_c	section chord force coefficient
c_d	section drag coefficient
$c_{d_{max}}$	maximum drag coefficient in dynamic stall, Fig. 3
c_l	section lift coefficient
$c_{l_{max}}$	maximum lift coefficient in dynamic stall, Fig. 3
c_m	section moment coefficient
$c_{m_{min}}$	minimum moment coefficient in dynamic stall, Fig. 3
c_n	section normal force coefficient
C_L	mean blade lift coefficient
C_T	thrust coefficient
k	reduced frequency, $\omega c/2V$
M	Mach number
r	blade radial location, ft; correlation coefficient
R	blade radius, ft
V	velocity, ft/sec
V_H	maximum level flight speed, ft/sec
y	oscillating wing spanwise location, in
Y	oscillating wing span, in
α	section angle of attack, deg
α_0	mean angle of attack, eq (4), deg
α_1	alternating angle of attack, eq (4), deg
μ	advance ratio
σ	solidity; standard deviation
ω	oscillatory frequency, rad/sec

		Form Approved OMB No. 0704-0188

Report Documentation Page

Public reporting burden for the collection of information is estimated to average 1 hour per response, including the time for reviewing instructions, searching existing data sources, gathering and maintaining the data needed, and completing and reviewing the collection of information. Send comments regarding this burden estimate or any other aspect of this collection of information, including suggestions for reducing this burden, to Washington Headquarters Services, Directorate for Information Operations and Reports, 1215 Jefferson Davis Highway, Suite 1204, Arlington VA 22202-4302. Respondents should be aware that notwithstanding any other provision of law, no person shall be subject to a penalty for failing to comply with a collection of information if it does not display a currently valid OMB control number.

1. REPORT DATE **2000**	2. REPORT TYPE	3. DATES COVERED **00-00-2000 to 00-00-2000**
4. TITLE AND SUBTITLE **Evaluation of Airfoil Dynamic Stall Characteristics for Maneuverability**		5a. CONTRACT NUMBER
		5b. GRANT NUMBER
		5c. PROGRAM ELEMENT NUMBER
6. AUTHOR(S)		5d. PROJECT NUMBER
		5e. TASK NUMBER
		5f. WORK UNIT NUMBER
7. PERFORMING ORGANIZATION NAME(S) AND ADDRESS(ES) **Army/NASA Rotorcraft Division,Army Aviation and Missile Command,Aeroflightdynamics Directorate (AMRDEC), Ames Research Center,Moffett Field,CA,94035**		8. PERFORMING ORGANIZATION REPORT NUMBER
9. SPONSORING/MONITORING AGENCY NAME(S) AND ADDRESS(ES)		10. SPONSOR/MONITOR'S ACRONYM(S)
		11. SPONSOR/MONITOR'S REPORT NUMBER(S)

12. DISTRIBUTION/AVAILABILITY STATEMENT
Approved for public release; distribution unlimited

13. SUPPLEMENTARY NOTES
Presented at the 26th European Rotorcraft Forum, The Hague, Netherlands, September 26-29, 2000

14. ABSTRACT
The loading of an airfoil during dynamic stall is examined in terms of the augmented lift and the associated penalties in pitching moment and drag. It is shown that once stall occurs and a leading-edge vortex is shed from the airfoil there is a unique relationship between the augmented lift, the negative pitching moment, and the increase in drag. This relationship, referred to here as the dynamic stall function, shows limited sensitivity to many parameters that influence rotors in flight. For single-element airfoils it appears that there is little that can be done to improve rotorcraft maneuverability except to provide good static clmax characteristics and the chord or blade number that is required to provide the necessary rotor thrust. The loading on a helicopter blade during a severe maneuver is examined and it is shown that the blade's dynamic stall function is similar to that obtained in two-dimensional wind tunnel testing. An evaluation of three-dimensional effects for flight and an oscillating wing in a wind tunnel suggests that the two problems are not proper analogues. The utility of the dynamic stall function is demonstrated by evaluating sample theoretical predictions based on semi-empirical stall models and CFD computations. The approach is also shown to be useful in evaluating multi-element airfoil data obtained from dynamic stall tests.

15. SUBJECT TERMS

16. SECURITY CLASSIFICATION OF:			17. LIMITATION OF ABSTRACT	18. NUMBER OF PAGES	19a. NAME OF RESPONSIBLE PERSON
a. REPORT **unclassified**	b. ABSTRACT **unclassified**	c. THIS PAGE **unclassified**	**Same as Report (SAR)**	**21**	

2   Introduction

McHugh and his colleagues measured the steady thrust of a 10-foot diameter CH–47B model rotor in the Boeing 20- by 20-Foot V/STOL Wind Tunnel to define the actual thrust limits of this rotor (Refs 1, 2). Their measurements are particularly useful as the rotor was designed with sufficient structural strength that the true aerodynamic thrust limit was obtained, that is, for any advance ratio and propulsive force, they increased the collective pitch until the thrust reached its maximum value and then reversed. The rotor thrust limit as a function of advance ratio that was obtained is shown in Fig. 1.
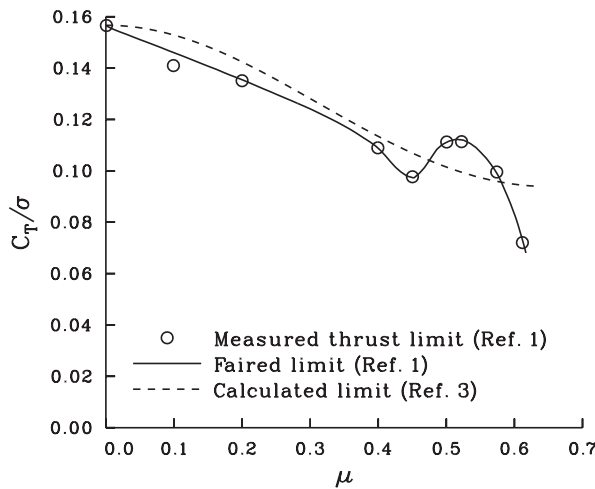

Figure 1. Comparison of measured and calculated limit rotor thrust coefficient as a function of advance ratio for a 10-foot diameter model rotor, $X/qd^2s = 0.05$.

Harris, in Ref. 3, has shown that the rotor thrust limit in forward flight, assuming roll moment balance, can be related to a mean blade airfoil lift coefficient as

$$\frac{C_T}{\sigma} = \frac{C_L}{6}\left(\frac{1 - \mu^2 + 9\mu^4/4}{1 + 3\mu^2/2}\right) \qquad (1)$$

At $\mu = 0$, eq (1) becomes the expected

$$\frac{C_T}{\sigma} = \frac{1}{6}C_L \qquad (2)$$

In Fig. 1, the mean value for C_L has been set to 0.94, and the Harris equation shows good agreement with the McHugh thrust boundary.

The problem of relating rotor thrust capability to airfoil section characteristics is more difficult than suggested by eq (1) when it is recognized that the rotor thrust limit is not dependent upon the maximum static

airfoil lift, but there is an unsteady or dynamic component that increases the rotor thrust capability (Ref. 4). Measurement of the rotor thrust of a full-scale H–21 rotor in the 40- by 80-Foot Wind Tunnel at Ames Research Center in the 1950s, by McCloud and McCullough (Ref. 5), demonstrated that the rotor was able to provide more thrust than would be calculated using just the airfoil static lift coefficient (Ref. 4). This additional thrust, achieved by what is now referred to as dynamic stall, has been the subject of extensive research over the past 40 years (Ref. 6, 7).

A fundamental problem for the rotor designer, then, is to what degree does the airfoil design affect the rotor's thrust capability in maneuvers, and probably more important, the increased pitching moment and power that accompanies the augmented lift associated with dynamic stall. The purpose of the present paper is to examine two-dimensional wind tunnel tests of a variety of helicopter airfoils and assess their dynamic stall performance. Flight data on a UH–60A in maneuvering flight will then be used to relate the wind tunnel measured characteristics to maneuver performance. A metric will be introduced, herein called the dynamic stall function, and it will be shown how this metric can be used to assess both theoretical prediction methods and experimental measurements.

3   Two-Dimensional Airfoil Tests

3.1 Ames Test Program

McCroskey and his colleagues tested eight airfoils in the NASA-Ames 7- by 10-Foot Wind Tunnel in the late 1970s and early 1980s (Refs. 8-10). Each airfoil was tested on the same dynamic test rig and, in general, the same range of test conditions was covered. The eight profiles tested are shown in Fig. 2.

The NACA 0012 airfoil is representative of the first generation of helicopter sections and has a symmetric profile. The AMES–01, Wortmann FX 69–H–098, SC1095, HH–02, VR–7, and NLR–1 are second generation airfoils and four of these are used in current production aircraft. The eighth section, the NLR–7301, is representative of a supercritical, fixed-wing section. Compared to the other seven airfoils it is characterized by a large leading-edge radius and large aft camber which results in large negative pitching moments at all angles of attack. The NLR–7301 is not considered suitable for use in helicopter applications, but was included in the test
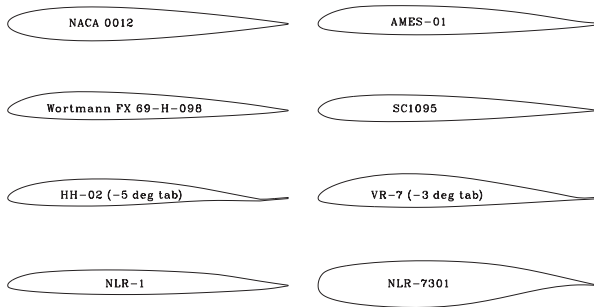
Figure 2. Eight airfoils tested in the NASA Ames 7- by 10-Foot Wind Tunnel (Refs. 8-10).

program to better understand the dynamic stall characteristics of fixed-wing airfoil sections with significantly different leading edge geometries.

The airfoil chord for each of the eight profiles was 24 in. The airfoils were mounted vertically in the test section of the 7- by 10-Foot Wind Tunnel such that the airfoils spanned the tunnel's shorter dimension. Thus the effective height to chord ratio was 5.0, based on the 10-foot width of the tunnel and the width to chord ratio was 3.5. Fifteen pressure transducers were mounted on the upper surface, ten were placed on the lower surface, and a single transducer was installed at the airfoil leading edge. The measured pressures were integrated to obtain the section forces, c_n and c_c, and the section moment, c_m. The measured angle of attack of the airfoil was used to convert these coefficients to the wind tunnel axes.

$$c_l = -c_c \sin \alpha + c_n \cos \alpha$$
$$c_d = c_c \cos \alpha + c_n \sin \alpha$$
(3)

The c_d calculated in this manner does not include the viscous drag, of course.

Dynamic stall data were obtained in the Ames tests by oscillating the airfoil in angle of attack around a mean value. The airfoil motion was defined as

$$\alpha(\omega t) = \alpha_0 + \alpha_1 \sin \omega t$$
(4)

Typically, test data were obtained for mean angles of 10 and 15 deg and alternating angles of 5 and 10 deg. Reduced frequencies varied from 0.02 to 0.20 and most of the data were obtained for a Mach number of 0.3, but with some data taken for Mach numbers as low as 0.04. The Reynolds number ranged from 400,000, at $M = 0.04$, to 4 million at $M = 0.3$. The number of test conditions varied from 49 for the Wortmann FX 69–H–098 to 121 for the NACA 0012. Not all of these test points are included here. For the NACA 0012 airfoil, a number of test points were obtained for quasi-static rather than dynamic stall

conditions, that is, the reduced frequency was approximately zero ($k < 0.005$), and these 21 conditions are not included. For the NLR–1 airfoil, a set of test cases were run with $\alpha_0 = -2$ deg and $\alpha_1 = 10$ deg and, therefore, dynamic stall occurred for negative lift conditions. Therefore, these eight test cases have also been excluded from the comparisons shown here. Finally, 13 test conditions for the NLR–7301 are excluded where α_0 was set near the static stall angle, and small values of the alternating angle of attack, $\alpha_1 = 2$ deg, were used to better understand this airfoil's flutter characteristics. None of these conditions indicated the shedding of a dynamic stall vortex and, in some cases, the airfoil remained stalled for the full cycle.

Section force and moment time histories are provided in Ref. 9 for each airfoil and each test condition. Figure 3 shows an example of the lift, drag, and moment loops for the NACA 0012 for a test condition that represents deep stall. Indicated on this figure are the maximum lift, the maximum drag, and the minimum moment during the oscillation. These extrema occur at slightly different angles of attack and are, therefore, not coincident in time. However, they are each related to the passage of the dynamic stall vortex along the airfoil and are representative of the maximum loading that occurs during a dynamic stall cycle.

The extrema from the dynamic stall loops for the eight airfoils tested at Ames are shown in Figs. 4 and 5. Figure 4 shows the maximum lift as a function of minimum moment, while Fig. 5 shows the maximum lift as a function of maximum drag. Most of these data were obtained without a boundary layer trip, but a number of test conditions were obtained with a boundary layer trip and are shown with a different symbol.

In general, each of the eight airfoils shows similar characteristics. That is, as additional lift develops on the airfoil in dynamic stall there is an associated increase in both the negative pitching moment and the pressure drag. For moments less than about –0.1, or drag values greater than about 0.1, the test data show that either one or two vortices are shed from the vicinity of the airfoil's leading edge, and these vortices are convected along the airfoil's upper surface and off the trailing edge. A single vortex is generally seen for moment values between –0.1 and –0.5, but at higher lift, two shed vortices are observed, one following the other. The relationship between lift, moment, and drag that is seen in Figs. 4 and 5 is a consequence of the convection of the dynamic stall vortices along the airfoil. This loading characteristic is herein termed the
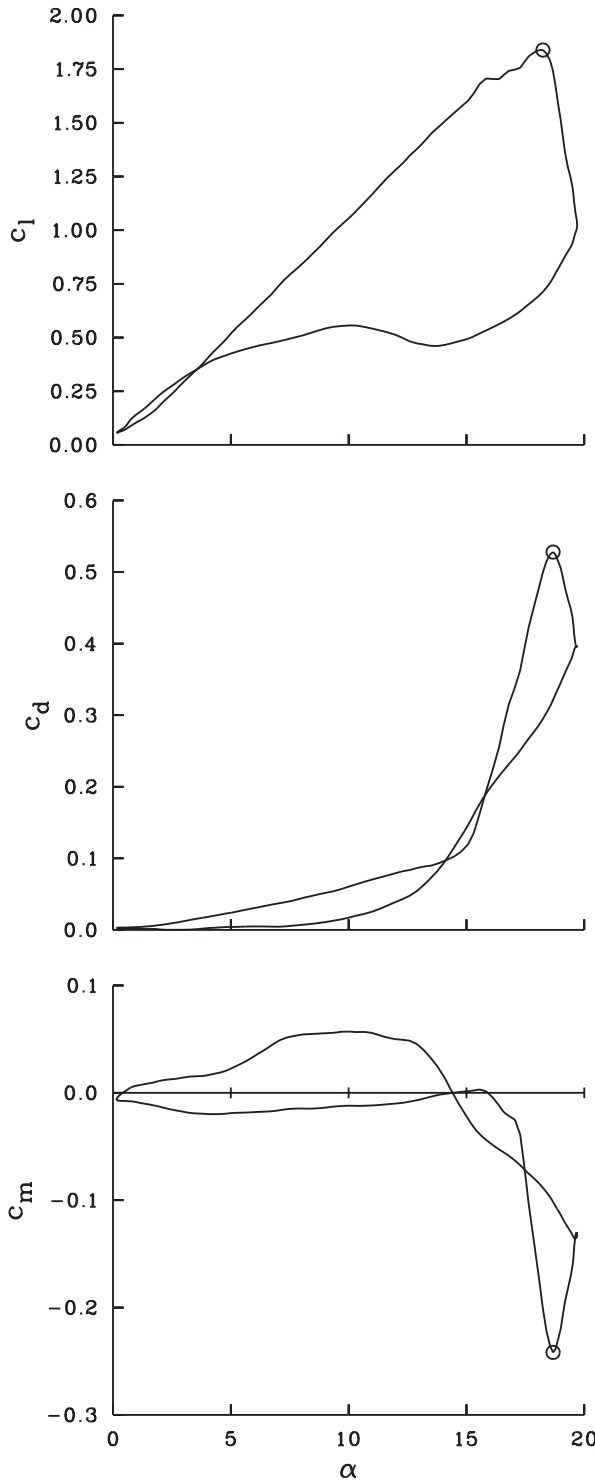
Figure 3. Dynamic stall test point for NACA 0012 from Ames tests; Frame 9302.

"dynamic stall function" and is used as a means of characterizing the loads on an airfoil caused by dynamic stall.

Figures 4 and 5 also include static airfoil characteristics for reference. As shown in Fig. 4 for the helicopter sections, the moment is close to zero over the normal range of airfoil lift and the moment becomes negative only after the airfoil stalls. Figure 5 includes the static airfoil drag measured using a wake survey (solid line) as well as the drag obtained from integration of the measured pressures (dotted line). Below stall, the drag values are very low, but once stall occurs there is a substantial increase in drag.

A comparison of the dynamic and static lift, drag, and moment in Figs. 4 and 5 indicates that as the zero moment or zero drag axis is approached, the dynamic stall function, as defined by these data, tends to approach the measured airfoil static $c_{l_{max}}$.

The dynamic stall function can be quantified by fitting a 2nd-order polynomial to the data, and the fitting polynomial is shown by dashed lines in Figs. 4 and 5. The fitting polynomials are defined as

$$c_l = a_0 + a_1 c_m + a_2 c_m^{\,2}$$
$$c_l = b_0 + b_1 c_d + b_2 c_d^{\,2} \tag{5}$$

The data obtained with a tripped boundary layer were not used for the fit as in some cases these data clearly show a dynamic stall function that differs from the untripped data, see Ref. 11. The polynomial coefficients defined by eq (5) are shown in Tables 1 and 2 along with two measures of dispersion: the coefficient of determination, r^2, and the standard deviation, σ.

3.2 Oscillating Wing Test

Piziali (Ref. 12) tested an oscillating wing in the same NASA-Ames 7- by 10-Foot Wind Tunnel as used by McCroskey and his colleagues. Test data were obtained for an NACA 0015 airfoil section in both two- and three-dimensional configurations. The wing had a span of 60 in and a chord of 12 in. Differential and absolute pressure transducers were installed at various span locations. For the two-dimensional tests, data were obtained at four span stations: three with differential pressure transducers arrays and one with an absolute pressure transducer array. The chordwise array of absolute pressure transducers was located at a span of $0.500Y$. At this station ten pressure transducers were mounted on the upper surface, eight were on the lower surface, and one was placed at the leading edge. The pressures were integrated to obtain the airfoil forces and these forces were converted to the wind tunnel axis system
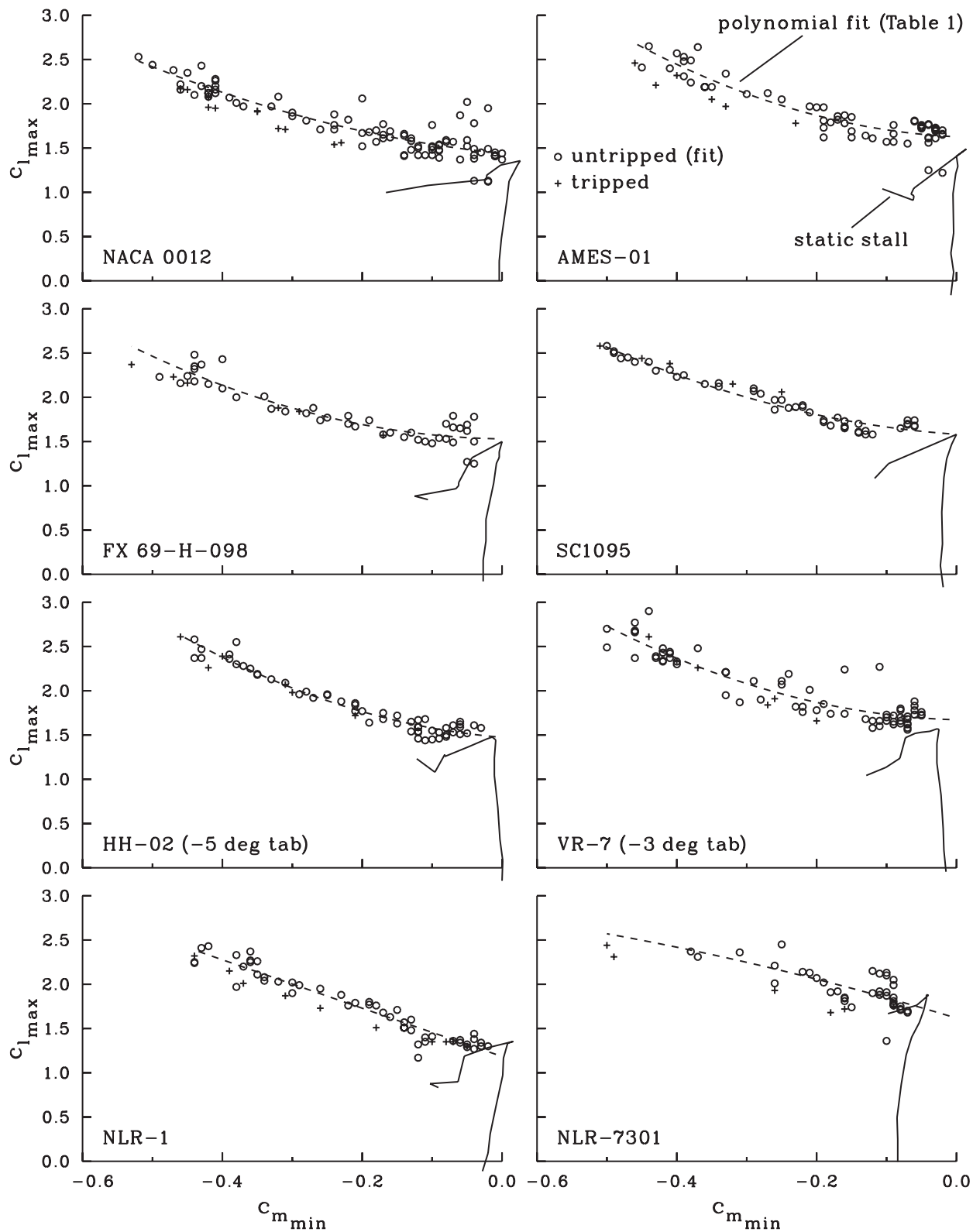
Figure 4. Maximum lift coefficient as a function of minimum moment coefficient for dynamic stall test data on eight airfoils from Ames tests. Polynomial fit of untripped data.
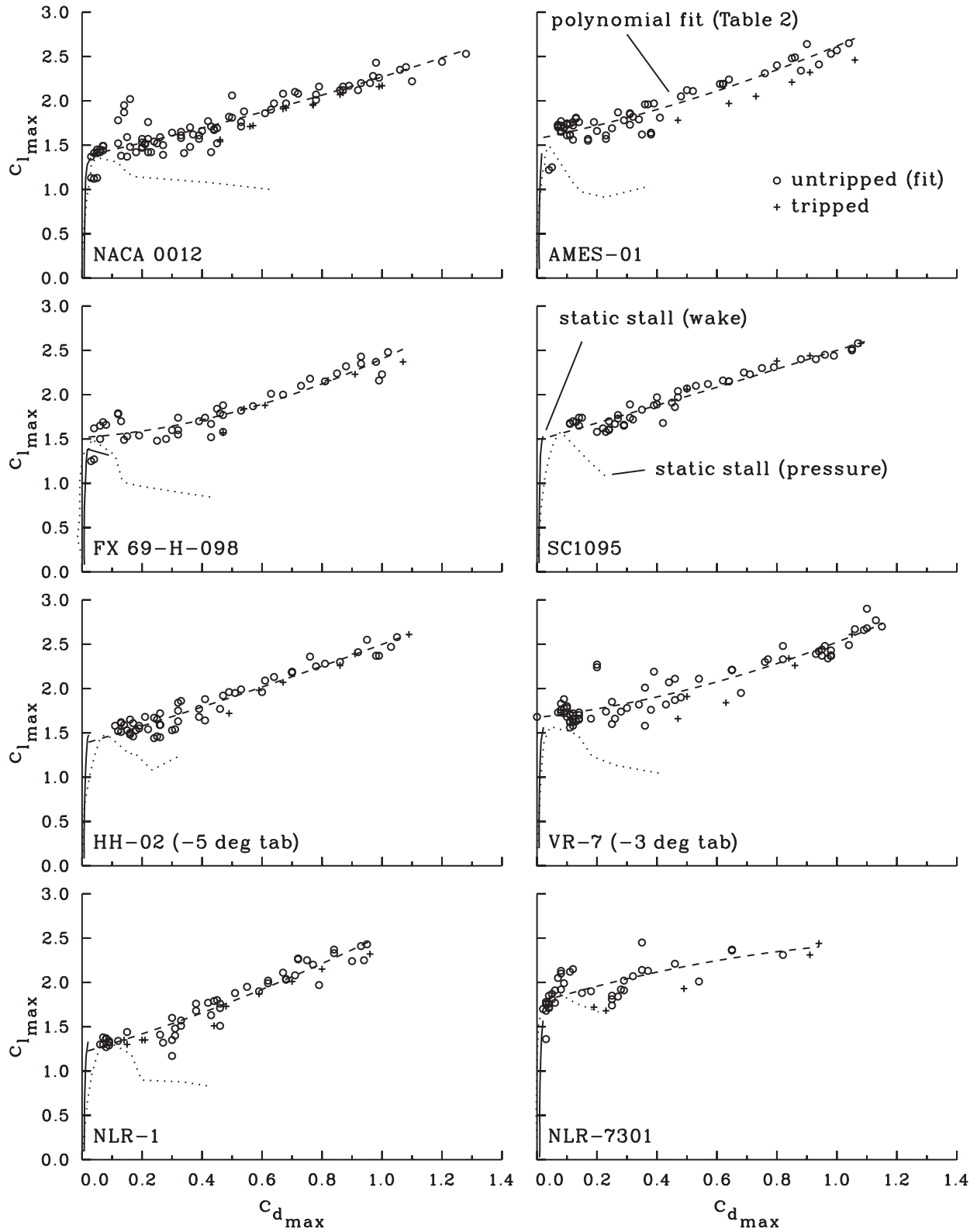
Figure 5. Maximum lift coefficient as a function of maximum drag coefficient for dynamic stall test data on eight airfoils from Ames tests. Polynomial fit of untripped data.

Table 1. 2nd order polynomial fit of dynamic stall function, lift as a function of moment.

AIRFOIL	a_0	a_1	a_2	r^2	σ
NACA 0012	1.439	-0.791	2.232	0.81	0.14
AMES–01	1.627	-0.361	4.210	0.85	0.13
FX 69–H–098	1.530	-0.107	3.519	0.84	0.12
SC1095	1.582	-0.532	2.869	0.95	0.07
HH–02	1.474	-0.643	4.054	0.95	0.08
VR–7	1.672	-0.229	3.773	0.84	0.14
NLR–1	1.184	-2.721	0.026	0.93	0.10
NLR–7301	1.618	-2.392	-0.973	0.53	0.15
NACA 0015	1.324	-0.342	3.538	0.73	0.07

Table 2. 2nd order polynomial fit of dynamic stall function, lift as a function of drag.

AIRFOIL	b_0	b_1	b_2	r^2	σ
NACA 0012	1.371	0.741	0.156	0.82	0.14
AMES–01	1.571	0.679	0.368	0.86	0.12
FX 69–H–098	1.516	0.238	0.649	0.85	0.12
SC1095	1.485	0.971	0.044	0.93	0.08
HH–02	1.373	0.997	0.129	0.93	0.09
VR–7	1.673	0.402	0.448	0.86	0.14
NLR–1	1.208	0.990	0.332	0.91	0.11
NLR–7301	1.769	1.010	-0.361	0.48	0.16
NACA 0015	1.336	-0.052	1.439	0.59	0.09

using eq (3).

Test data were obtained for mean angles of attack of 4, 9, 11, 13, 15, and 17 deg, and alternating angles of 2, 4, and 5 deg. The reduced frequencies tested ranged from 0.04 to 0.20. The Mach number was approximately 0.3 and the Reynolds number about 2 million. Ninety-eight two-dimensional test points were obtained and include both untripped and tripped data. Forty-two of these points are excluded in the present analysis as the maximum angle of attack was less than the static stall angle of approximately 13.5 deg. An additional eight points obtained at angles of 17±2 deg are also excluded as these test conditions showed evidence of stalled flow over the entire range of angles of attack.

The two-dimensional data for the NACA 0015 airfoil obtained from the span station with absolute pressure transducers are shown in Fig. 6 with the untripped and tripped data points indicated by different symbols. The dynamic stall functions for these data do not extend as far as was observed in the Ames tests for the other airfoils and this indicates that the dynamic stall vortex strength is somewhat reduced. Polynomials have been fitted to these data and are included in Tables 1 and 2 with the data from the Ames tests.
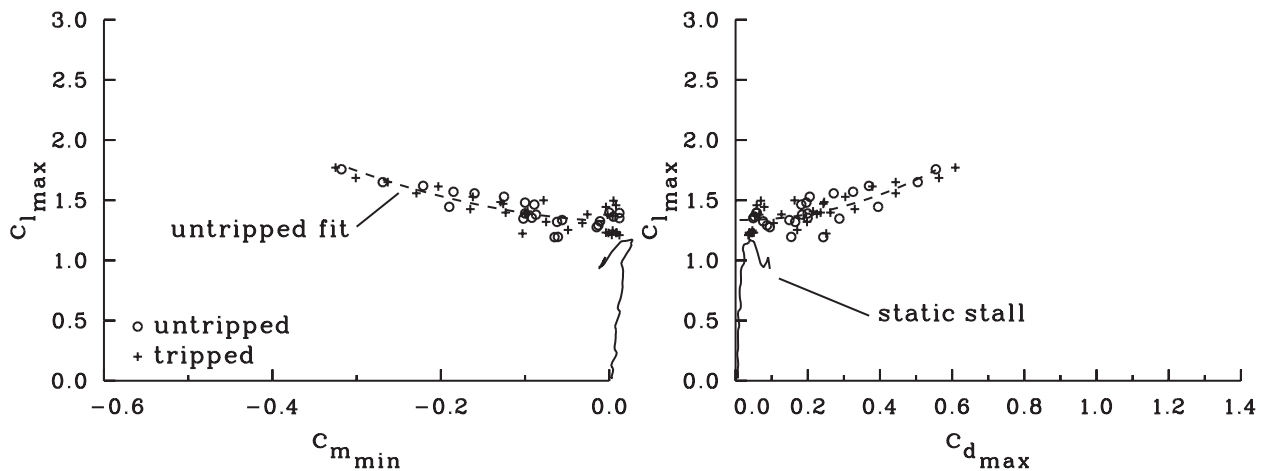
Figure 6. Maximum lift coefficient as a function of minimum moment and maximum drag coefficients from test of NACA 0015 airfoil. Polynomial fit of untripped data.

3.3 Supporting Tests

Oscillating airfoil data are available from a number of sources that can be compared with the Ames test data in Figs. 4 and 5. These comparisons are of value to confirm the general behavior of the dynamic stall function and also to examine additional test conditions beyond the range of parameters examined in the Ames tests.

St. Hilaire et al. tested an NACA 0012 airfoil in the Main Wind Tunnel at the United Technologies Research Center (UTRC) and reported the results in Ref. 13. The primary purpose of this test was to examine the effects of sweep on blade stall, but the data obtained for unswept conditions can be compared directly with the Ames data. For these tests, twelve absolute pressure transducers were installed on the upper surface and eight were installed on the lower surface. The section chord was 16 in. Lift, drag, and moment were obtained by integrating the measured pressures and the resulting forces were converted to wind tunnel axes using eq (3). Mean angles of attack ranged from 5 to 15 deg, and alternating angles were either 5 or 10 deg. Reduced frequencies varied over a range of 0.02 to 0.20. Data were obtained for Mach numbers of 0.1, 0.3, and 0.4 (Reynolds numbers of 920,000, 2.8 million, and 3.7 million), but only data at $M = 0.1$ and 0.3 are shown here, as this is the range of Mach numbers used in the Ames tests. Figure 7 compares the UTRC measurements with the polynomials based on the Ames data from Tables 1 and 2. The scatter in the Ames data is represented by $\pm 1\sigma$ boundaries. The UTRC data generally show good agreement with the

Ames tests, although the four points obtained at $M = 0.1$ lie outside the Ames 1σ boundary.

Two sources of dynamic stall data have been examined for the VR–7 airfoil. The first data set is from the Centre D'Essais Aeronautique de Toulouse (CEAT) wind tunnel in Toulouse, France, and was obtained under the auspices of the U.S./France Memorandum of Understanding for Cooperative Research in Helicopter Aeromechanics. A general description of the test procedures used with this wind tunnel and test rig are provided in Ref. 14. The second data set is from the Ames water tunnel (Ref. 15). The CEAT data were obtained in a conventional atmospheric wind tunnel using a model with a 40-cm chord. Thirteen differential pressure transducers were installed on the airfoil and, hence, only normal force and moment coefficients are available. The data from the water tunnel tests were obtained on a model airfoil of four in chord mounted in the water tunnel's 8.3- by 12-inch test section. The lift, drag, and moment were measured with an external balance with corrections for friction, but not for inertial loads, which were considered negligible (Ref. 15). The CEAT tests examined mean angles of attack of 10 and 15 deg, and alternating angles of 5 and 6 deg. Reduced frequencies varied from about 0.02 to about 0.23. The Mach number ranged from about 0.12 to 0.3, and the Reynolds number varied from 1 million to just under 3 million. The water tunnel tests included mean angles of attack of 5, 10, and 15 deg, and alternating angles of 10 deg. The reduced frequencies varied from 0.025 to 0.20. The Mach number was zero, of course, and the Reynolds number ranged from 100,000 to 250,000. The data
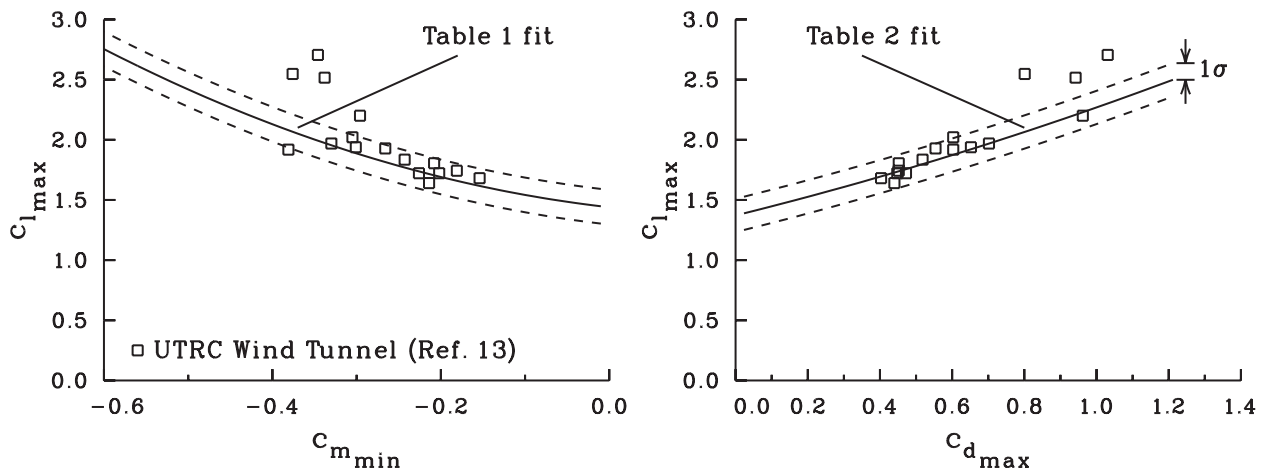
Figure 7. Comparison of dynamic stall extrema from UTRC tests of NACA 0012 airfoil with polynomial fits of Ames test data.
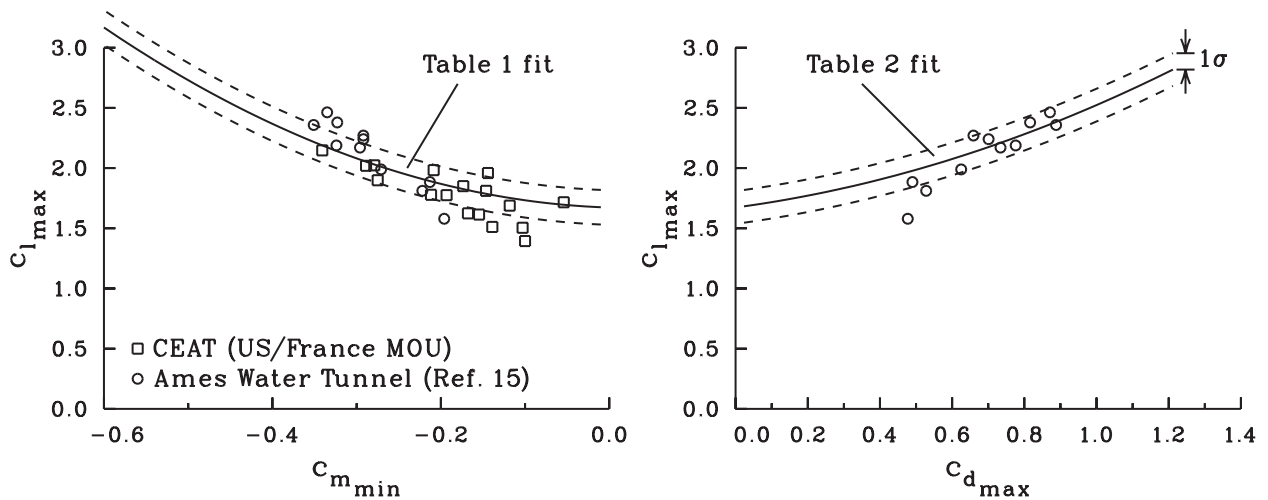

Figure 8. Comparison of dynamic stall extrema from CEAT tests and from Ames water tunnel tests of VR–7 airfoil with polynomial fits of Ames test data.

from these two tests are compared with the Ames data in Fig. 8.

The data from both the CEAT wind tunnel tests and the Ames water tunnel tests show good agreement with the Ames wind tunnel data. Since the CEAT data were obtained using differential pressure transducers, only the normal force coefficient, c_n, and not the lift coefficient, c_l, is computed. However, there are only slight differences between these two coefficients during dynamic stall (Ref. 11) and these differences do not affect the comparison shown here. The water tunnel test results show very good agreement with the wind tunnel data despite the large difference in Reynolds number. This interesting result suggests that the dynamic stall vortex, that

dominates the loading on the airfoil during dynamic stall, is relatively insensitive to Reynolds number.

Dynamic stall data were obtained for the SC1095 (and SC1094 R8) airfoil in the UTRC facility using the same procedures and test rig as for the NACA 0012 tests discussed above. Of these data, five lift-moment loops have been published by Gangwani (Ref. 16). The remainder of these data remain unpublished. Mean angles of attack of 9, 12, and 15 deg were tested with alternating angles of 8 deg. The reduced frequencies ranged from 0.10 to 0.12, the Mach number was 0.3, and the Reynolds number was about 2.8 million. The five SC1095 test points are compared with the Ames test data in Figure 9. The UTRC data agree quite well with the Ames data, with three of the points within the 1σ boundary and two
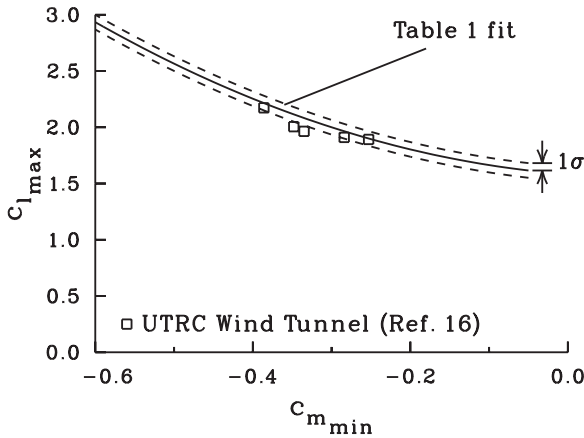
38.9

Figure 9. Comparison of dynamic stall extrema from UTRC tests of SC1095 airfoil with polynomial fits of Ames test data.

Figure 10. Comparison of dynamic stall extrema from BSWT tests of NLR–1 airfoil with polynomial fits of Ames test data.

slightly outside. Very little scatter was observed in the Ames test of this airfoil.

An extensive set of unsteady airloads and dynamic stall data have been obtained for the NLR–1 airfoil (Ref. 17, 18). The test data were obtained in the Boeing Supersonic Wind Tunnel, using a two-dimensional subsonic insert. The airfoil chord was 6.38 in and, with the installed subsonic insert, the test section was 36 in high and 12 in wide. Seventeen differential transducers were installed on the model and the pressures were integrated to provide c_n and c_m. The data were obtained over a Mach number range from 0.2 to 0.7 and for numerous combinations of mean and alternating angles of attack, both stalled and unstalled. For comparison with the Ames data, only test points with $M = 0.2$ or 0.3 are used. In addition, test conditions have been excluded in those cases where the sum of the mean and alternating amplitude is less than the static stall angle of 12.4 deg.

Figure 10 compares the data from Refs. 17, 18 with the Ames tests. The Reynolds number in the Boeing tests is about 25% higher than the Ames tests. The range of mean and alternating angles of attack is similar to the Ames tests. The range of reduced frequencies for the Boeing tests extends to 0.35, and this is beyond the range tested at Ames. The envelope of maximum c_n and minimum c_m for the Boeing test is similar to that obtained at Ames and the majority of test points fall within the $\pm 1\sigma$ bounds of the Ames data. Note again, as in the case of the CEAT data for the VR–7 airfoil, these data are for the normal force coefficient rather than the lift coefficient.
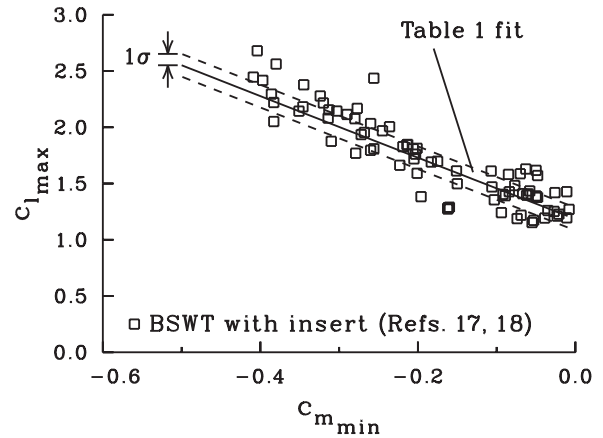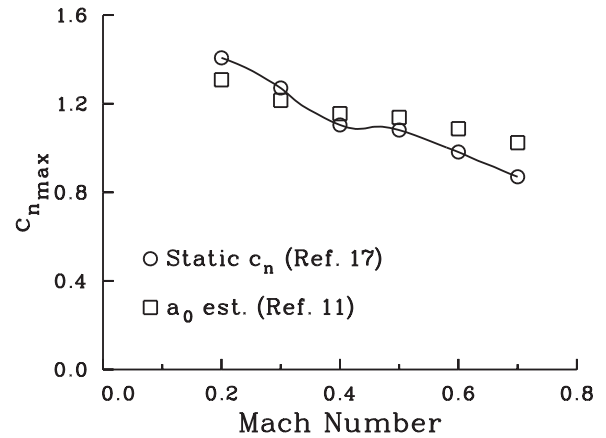

Figure 11. Comparison of the measured NLR–1 static maximum normal force coefficient and an estimate of the a_0 intercept from the dynamic stall data.

The dynamic stall data obtained on the NLR–1 section are of particular interest as they were obtained over a large range of Mach numbers. The effects of Mach number on the dynamic stall function have been examined in Ref. 11. As Mach number increases the dynamic stall function maintains roughly the same shape as shown in Fig. 4, but is reduced in extent. That is, at higher Mach numbers the maximum c_n and minimum c_m obtained in the test are reduced. In addition, there is a slight shift downwards in the dynamic stall function with increasing Mach number. This downward shift is shown in Fig. 11, where an estimate of the polynomial a_0 coefficient (dynamic stall function intercept) is shown as a function of Mach number. Interestingly, the static $c_{n_{max}}$ measured on this airfoil

38.10

(Ref. 17) shows a similar decrease with increasing Mach number.

3.4 Airfoil Comparisons

The dynamic stall functions shown in Figs. 4–6 exhibit similar behavior and, as the function approaches zero moment or zero drag, the lift coefficient approaches the airfoil static $c_{l_{max}}$. Figure 12 shows the dynamic stall function intercepts, that is a_0 and b_0, as functions of the measured static $c_{l_{max}}$ of the airfoils (Refs. 8, 12). As expected, the a_0 and b_0 intercepts are nearly the same for each airfoil and, for most of the helicopter sections, the intercepts show a lift increment over the static $c_{l_{max}}$ of 0.05 to 0.12. The intercept values are largely defined by the measurements for light stall conditions where no dynamic stall vortex is shed and, in this sense, the intercepts indicate the incremental lift that can be obtained in unsteady motion without a moment or drag penalty. The fixed-wing section, the NLR–7301, has a considerably better $c_{l_{max}}$ than any of the helicopter sections, but its dynamic stall function shows an intercept well below the $c_{l_{max}}$ which indicates that the airfoil will not obtain any lift increment for unsteady motion. The NLR–1 airfoil, which is a helicopter section designed for good advancing blade transonic characteristics, does not show good dynamic stall performance and the intercept values are below the static $c_{l_{max}}$.
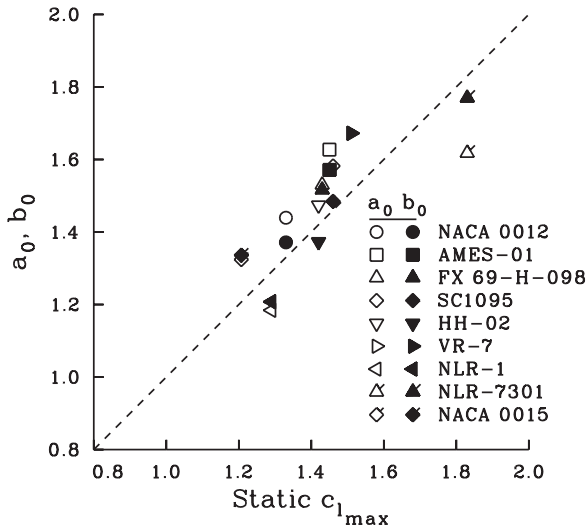

Figure 12. Comparison of the a_0 and b_0 intercepts from dynamic stall tests with the measured static maximum lift coefficient from tests of nine airfoils.

The dynamic stall functions of the nine airfoils are compared in Fig. 13. Except for the NLR–1 and NLR–7301, the form of the dynamic stall function for these airfoils is similar. The poorest performance is for the NACA 0015 profile, which is thicker than the other helicopter sections. The thinner NACA 0012 profile shows better performance than the NACA 0015, and the second generation airfoils are, mostly, substantially better than the symmetric NACA 0012. The NLR–1 airfoil shows relatively good performance in deep stall but, as noted previously, is deficient in light stall conditions. The fixed-wing section, the NLR-7301, starts with a higher a_0 and b_0 intercept than the other airfoils, but there is less of an increase in lift as the stall becomes more severe.

4 Dynamic Stall in Maneuvering Flight

The dynamic stall function based on two-dimensional wind tunnel data provides a useful means of evaluating the dynamic stall performance of various helicopter airfoil sections. A question of interest, then, is to what extent can the dynamic stall function be used to quantify the airfoil performance during flight maneuvers. This section examines this question, using flight data obtained on a UH–60A, and also looks at three-dimensional effects.

4.1 UH–60A Flight Test Data

Reference 19 examined dynamic stall on a highly-instrumented UH–60A helicopter for three conditions: a level flight case at high altitude, a diving turn at high load factor, and the UTTAS pull-up maneuver. This examination demonstrated that dynamic stall is remarkably similar for all of these flight conditions and, in general, can be characterized by the shedding of a vortex from near the leading edge of the blade, just as has been observed in two-dimensional wind tunnel testing.

The UTTAS pull-up maneuver from Ref. 19 (Counter 11029) was re-examined to obtain maximum c_n and c_m values from the flight data that correspond to the extrema obtained from the two-dimensional tests. Data were examined at six radial stations from $0.675R$ to $0.99R$. The test maneuver is basically a symmetric pull-up that has been modified so that entry is made from level flight at V_H. For the case here, a load factor of 2.1g was obtained during the pull-up. The measured oscillatory pitch-link loads in this maneuver are shown in Fig. 14. In this figure each symbol represents one revolution of the
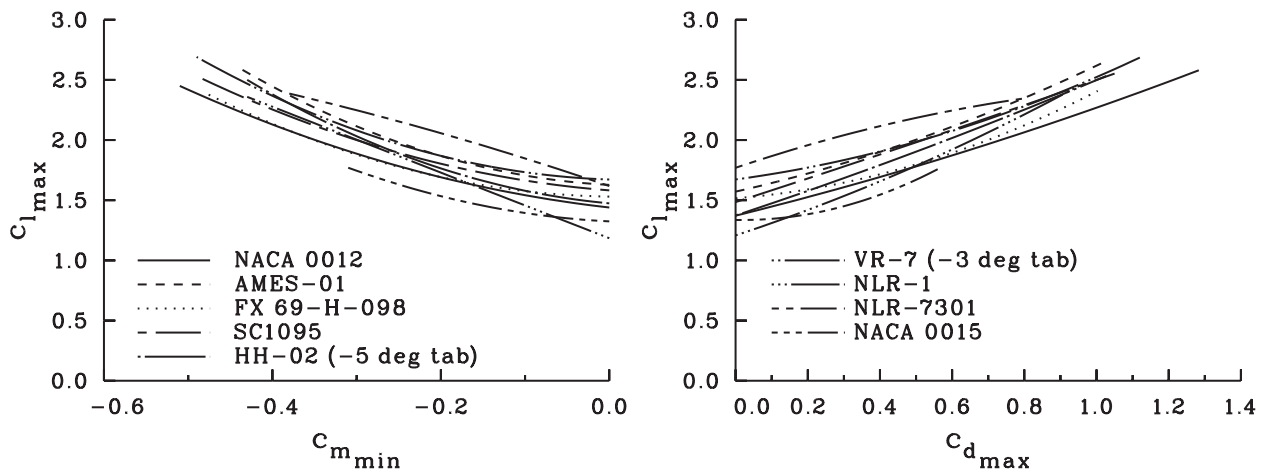
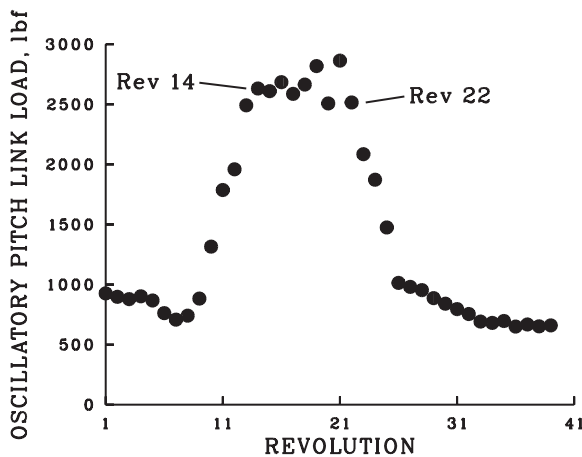*Figure 13. Comparison of dynamic stall function for nine airfoils.*

Figure 14. UH–60A oscillatory pitch-link loads in the UTTAS pull-up (Ref. 19).

Figure 15. Rotor disk map showing dynamic stall cycles on UH–60A rotor for Rev 14.

rotor. At the maneuver entry point, the oscillatory loads are just under 1000 lb and, then, at about Rev 09, the loads rapidly increase until they reach a plateau at about Rev 14. These loads are maintained through Rev 22 for a duration of a little over two seconds and then rapidly return to level flight values. This maneuver is particularly useful for comparison purposes as there are generally one to three cycles of stall during each revolution from Rev 08 to Rev 25 and this provides many c_n–c_m pairs to use in defining the dynamic stall function.

Figure 15 provides a rotor disk map of the dynamic stall events for Rev 14 during the pull-up maneuver. The azimuth associated with each stall event is defined as the mean of the azimuth at the c_n
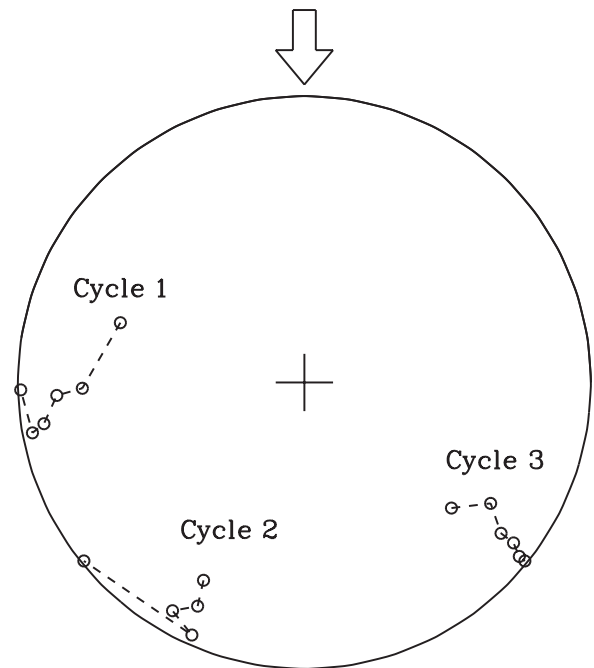
peak (lift stall) and the azimuth at the c_m minimum (moment stall). The first stall event occurs on the retreating side of the rotor prior to 270 deg. The dynamic stall for this first cycle initially occurs inboard and then moves outboard towards the tip. The second cycle occurs near the rear of the disk and, except for the most outboard station, the stall occurs simultaneously at all radial stations. The third cycle occurs at about 45 deg in the first quadrant of the

rotor and, as with the second cycle, is simultaneous at all radial stations.

All of the dynamic stall extrema for the UTTAS pull-up are plotted on Fig. 16 and each of the three cycles is indicated by a different symbol. Each revolution (see Fig. 14) provides up to three extrema for each radial station and there are approximately 17 revolution over the course of the maneuver which results in 267 extrema. Included in Fig. 16 is the SC1095 dynamic stall function from the Ames tests. Although the trend of the flight test data is similar to the dynamic stall function from two-dimensional tests, the scatter is substantially increased. The standard deviation of the flight data, relative to a fitting polynomial, is about 0.31, where the standard deviation for the wind tunnel test data is 0.07. Some of this scatter is caused by the significant range of Mach numbers in these data, from $M = 0.2$ to $M = 0.8$. In addition, the airfoil at the two inboard stations is the SC1094 R8 and its stall characteristics may be different from the SC1095. An approximate means of correcting for Mach number effects has been examined in Ref. 11. The correction was made based on static $c_{l_{max}}$ and this reduced the standard deviation to 0.25, but this scatter is still well above the two-dimensional results.
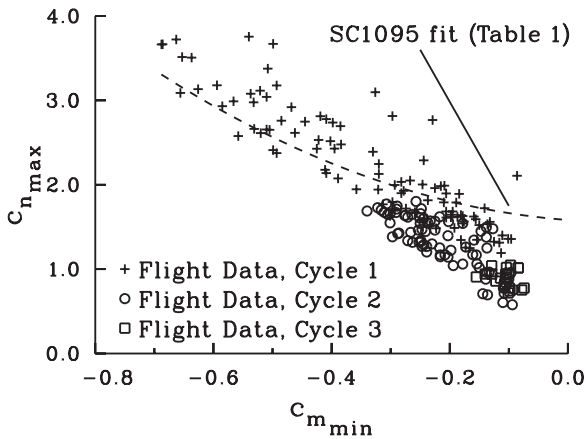

Figure 16. Dynamic stall extrema during UTTAS pull-up maneuver for UH–60A compared to SC1095 dynamic stall function.

4. 2 Three-Dimensional Effects

The lift and moment extrema that occur in the first dynamic stall cycle of each revolution are examined in Fig. 17 to see how the dynamic stall behavior changes near the blade tip. As noted previously, this first stall cycle occurs at the end of the third quadrant at about 270 deg. Data for each of the six radial stations are plotted separately and, for each subplot, the individual data points represent different revolutions during the flight maneuver. A 2nd-order polynomial based on the flight data is shown in Fig. 17 and compared to the SC1095 polynomial from Table 1. Each figure also includes the static stall characteristic measured in two-dimensional tests (Ref. 8). At the two most inboard stations, the flight data are 0.2 to 0.6 above the two-dimensional characteristic. The airfoil at these stations is the SC1094 R8, which is similar to the SC1095 but has additional camber or droop at the nose. No wind tunnel dynamic stall test data are available for this airfoil so it is not known whether the difference between the flight data and SC1095 dynamic stall function is because of the different airfoil characteristics or for other reasons.

The flight data at 0.865R, which is about two chords in from the tip, show good agreement with the Ames test results. At 0.92R, about one and a quarter chords in from the tip, the flight data show good agreement with the Ames tests at the edge of the deep stall region, but are somewhat lower in light stall. At 0.965R, a half chord from the tip, the flight data show less lift in stall than would be predicted from the Ames data and similar behavior is seen at 0.99R, which is about 16% of a chord from the tip.

The primary effect of three-dimensional flow, as observed for the first stall cycle during this maneuver, appears to be a slight reduction in the dynamic stall function for the radial stations within one chord of the blade tip. An examination of the blade pressure data (Ref. 19) shows that the dynamic stall vortex during this first cycle is clearly in evidence at each of these radial stations.

Piziali's oscillating wing data can be used to examine three-dimensional effects in a manner similar to the flight test data. Figure 18 shows data from the Ref. 12 experiments where, as in the two-dimensional tests, data are only included where the combined steady and alternating angle of attack exceeds the static stall angle. Data are shown at seven spanwise stations and a polynomial fit is included for the three-dimensional data as well as the two-dimensional fit from Table 1. The static data included in each figure are from three-dimensional, quasi-static tests and therefore differ at each spanwise station.

Inboard on the wing, very good agreement is observed between the two-dimensional and three-dimensional characteristics. At 0.800Y, which is one chord from the tip, the wing data follow the two-dimensional characteristics, but it appears that a
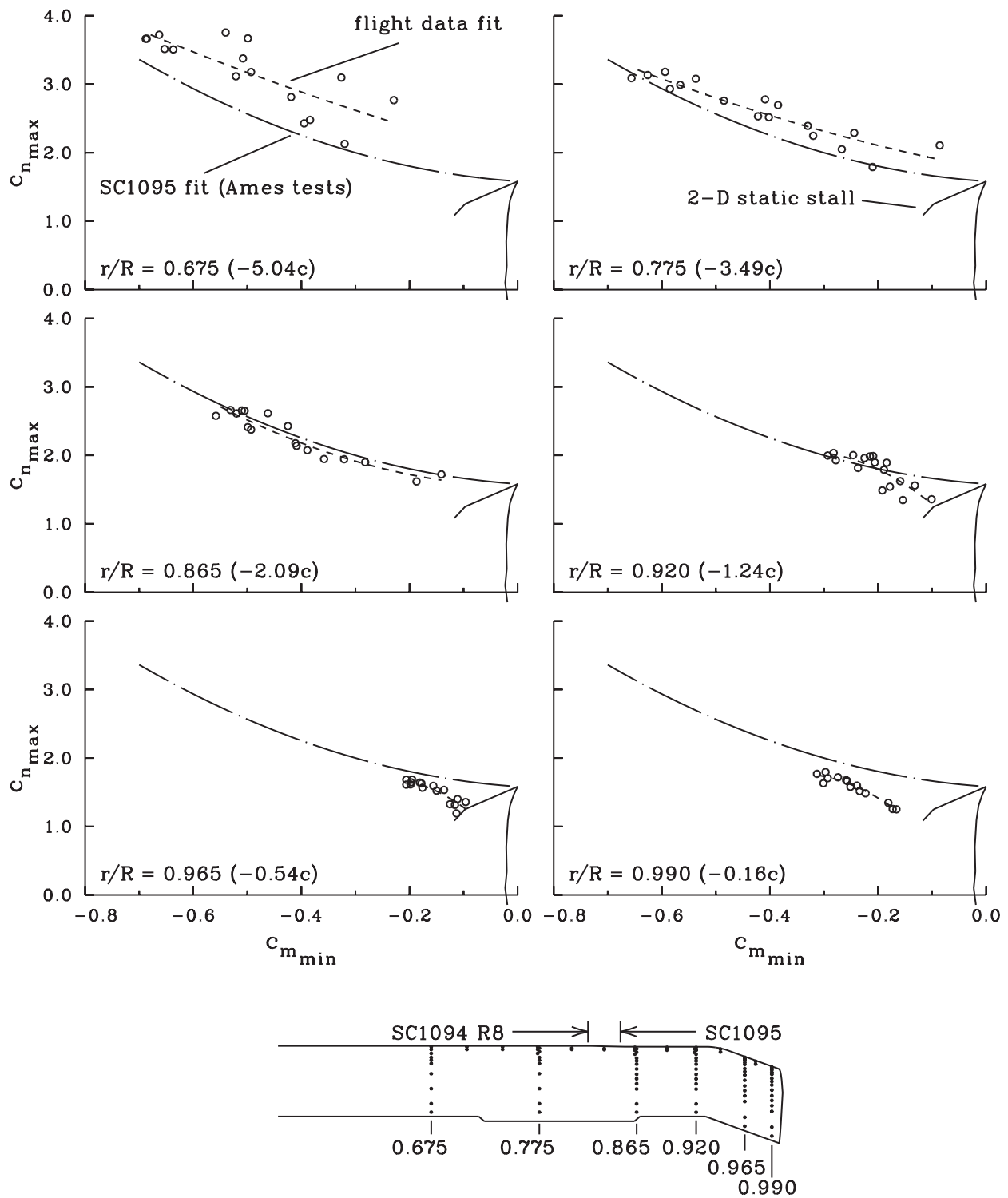
Figure 17. Dynamic stall extrema, for first stall cycle, measured at individual radial stations during UTTAS pull-up compared with SC1095 dynamic stall function.
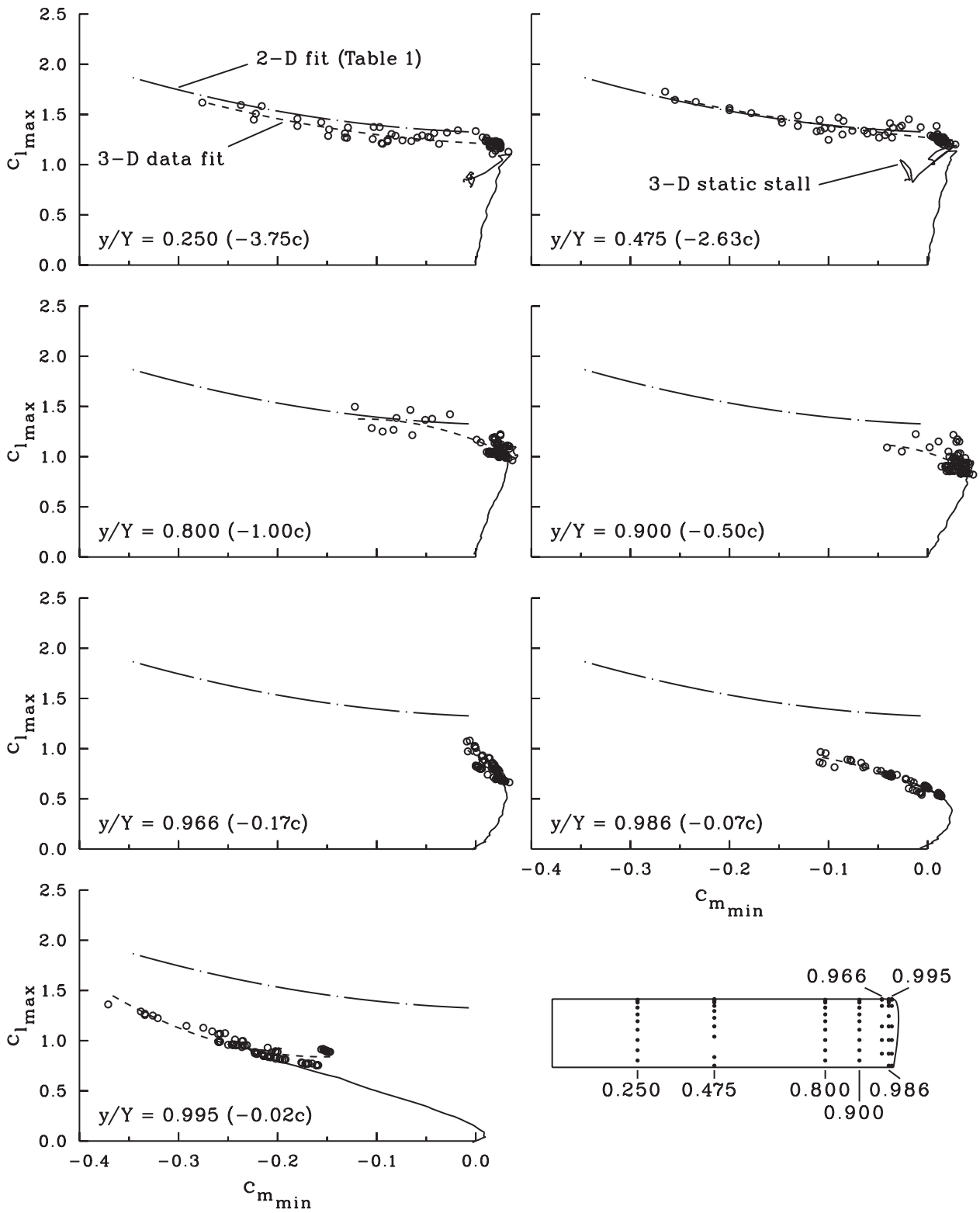
Figure18. Dynamic stall extrema measured on oscillating wing compared with NACA 0015 dynamic stall function.

number of the test points are unstalled, which suggests that the vortex strength is reduced at this station, compared to the two-dimensional case. At $0.900Y$ and $0.966Y$, no dynamic stall occurs and there is no indication in the pressure data that a dynamic stall vortex is being shed at this location. The data at $0.966Y$ are 17% of chord inboard from the tip and are comparable, therefore, with the data at $0.99R$ on the UH–60A rotor. Further outboard on the wing, at $0.986Y$ and $0.995Y$, the character of the lift and moment data change and the unsteady data agree quite closely with the data obtained for these locations in quasi-static tests. The lift and moment behavior at these outboard stations is a result of tip vortex formation, not a shed dynamic stall vortex.

The comparison shown here, between dynamic stall on a helicopter blade in flight and on an oscillating wing in a wind tunnel, shows similarities and differences. Inboard, both tests show that the dynamic stall behavior is very similar to that observed in two-dimensional tests. Within one or two chords of the blade or wing tip, however, the two test data sets differ. For the helicopter rotor blade, a shed dynamic stall vortex is clearly observed for all of the outer blade stations. Within a chord of the tip, the flight data show a small reduction in the dynamic stall function, while the basic character is similar to that observed in two-dimensional tests. The oscillating wing, on the other hand, indicates that a shed dynamic stall vortex is no longer present within a chord of the oscillating wing tip. The difference in the three-dimensional behavior between the helicopter and oscillating wing may be caused by differences in the radial velocity distribution or possibly other factors. The oscillating wing data remain a valuable resource in the development and testing of theoretical methods. However, as an analogue for dynamic stall on a helicopter blade in flight, the oscillating wing data do not appear suitable.

5 Dynamic Stall Function as a Metric

It has been shown here that the dynamic stall function can be used to evaluate airfoil dynamic stall performance from two-dimensional wind tunnel test data and that these characteristics are related to the measurements obtained on a helicopter during a maneuver. The dynamic stall function can also be used as a means of evaluating theoretical calculations or experimental measurements of novel airfoil designs.

5.1 Semi-empirical Models

Most comprehensive analyses used in the helicopter industry, government agencies, and academia use some form of lifting-line theory to calculate the aerodynamic loads on the rotor. In these analyses the steady aerodynamic forces and moment are based on tables or formulae from two-dimensional wind tunnel tests. The steady data are then modified to account for unsteady aerodynamics in the calculation of the loading. For angles of attack beyond the static stall angle, this approach underpredicts the aerodynamic loads and some form of semi-empirical dynamic stall model is used to provide the lift, drag, and moment as a function of angle of attack. The dynamic stall function can be used to check these models and one example is shown here.

The comprehensive analysis CAMRAD II includes five semi-empirical dynamic stall models (Ref. 20). These include the models used by Boeing (Ref. 21) and Johnson (Ref. 22), which are simpler models with few parameters to fit; the Leishman-Beddoes model (Ref. 23); and two ONERA models: the Edlin method developed by Tran and Petot (Ref. 24), and the Hopf Bifurcation model developed by Truong (Ref. 25). As each of the models is semi-empirical it is necessary to adjust or identify the model parameters based on test data. This has been done within CAMRAD II for the NACA 0012 airfoil, but not for other airfoils. Thus, it is expected that these models will provide a better prediction of the NACA 0012 characteristics than for other airfoil sections.

The predictions of the five models are compared with single test points for the NACA 0012 and SC1095 sections in Fig. 19. The two test points represent moderate to fairly severe stalled conditions. Most of the models provide a reasonable prediction of the maximum lift, but are substantially less accurate in predicting the minimum moment. In particular, the Boeing and ONERA Edlin models show a significant underprediction of the negative moment. The other models show poor-to-fair agreement in moment. Although it was anticipated that the predictions for the NACA 0012 would be better than for the SC1095, since the semi-empirical parameters in the models are based on NACA 0012 test data, this is not the case.

Since only one stall condition was evaluated in Ref. 20, an assessment of the semi-empirical models is difficult. An appropriate evaluation should include not only moderate stall conditions, as shown here, but also a light stall case and a severe, deep stall case.
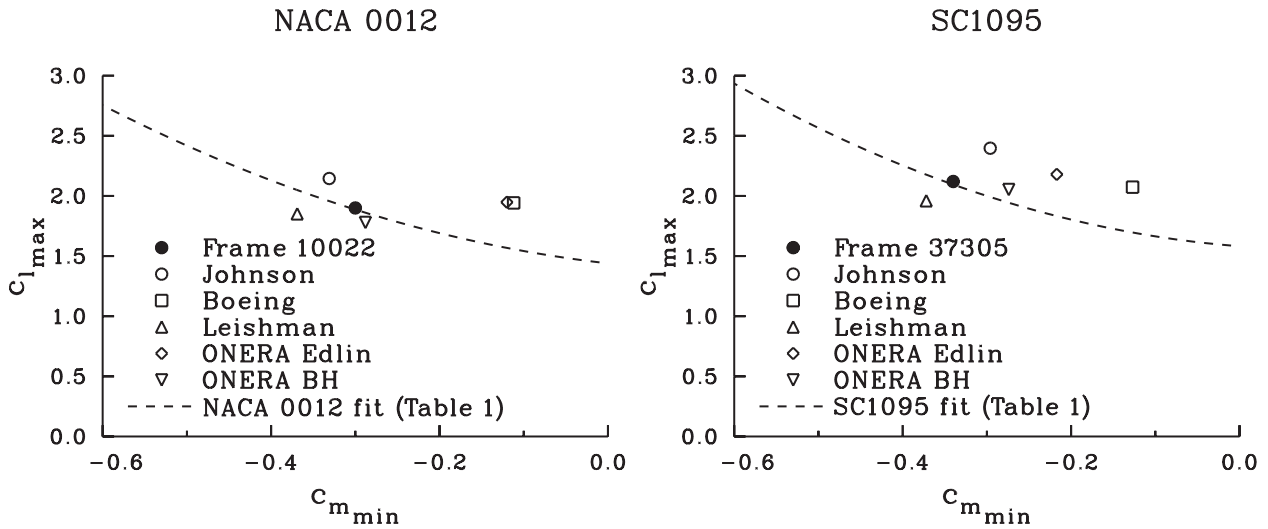
Figure 19. Comparison of synthesized data for NACA 0012 and SC1095 profiles using five semi-empirical models (Ref. 20).

5.2 CFD Models

Numerous numerical methods have been developed for the direct calculation of dynamic stall on an oscillating airfoil and this approach remains an exciting challenge for investigators interested in classical fluid mechanics. These methods, presently, are at a research or pilot stage and there has been no anticipation of their use within the design process. Eventually, however, it is envisioned that the best of these methods will show some utility in the development of semi-empirical models used within the comprehensive analyses. One example of a Navier-Stokes prediction for a case from the NACA 0012 data obtained at Ames is shown here.

Rouzaud and Plop have reported the development of a Reynolds-averaged, Navier-Stokes solver at ONERA (Ref. 26). They have examined the effects of two turbulence models: those of Baldwin and Lomax, and Launder and Sharma. They have compared their analysis with a severe stall case for the NACA 0012 from the Ames tests. These predictions, along with the data point from the Ames tests, and the polynomial fits from Tables 1 and 2, are compared in Fig. 20. The calculations with the Baldwin-Lomax model severely overpredict the moment and the drag is also high. However, the prediction using the Launder-Sharma model provides good results. In this sense, the Launder-Sharma model passes the necessary condition that there must be a good prediction of the extrema. However, an examination of the time behavior of the coefficients

in Ref. 26 shows that the extrema occur over a very short range of time steps compared to the data and there is an associated phase shift. In addition, the experimental case used here included two shed vortices (Ref. 9) and the Navier-Stokes calculations indicate only a single vortex.

Simple changes to the boundary layer, as induced by a boundary layer trip, for example (Ref. 11), do not show a substantial effect on the dynamic stall function for experimental measurements. The ONERA calculations show a more significant influence of the boundary layer in the example here and this emphasizes the necessity of extensive experimentation with computational models before their utility can be demonstrated.

5.3 Experimental Tests of Multi-element or Variable Geometry Airfoils

As shown in this paper, conventional, single-element airfoils show similar dynamic stall characteristics. Although it is expected that small gains in performance, in terms of dynamic stall, may be obtained through careful design, substantial improvements do not appear feasible. Improved dynamic stall performance using multi-element or variable geometry airfoil designs, however, may be possible. Two multi-element airfoil designs have been tested in the Ames water tunnel (Ref. 15, 27) and their performance here is compared to the dynamic stall function to illustrate the utility of this approach as a means of evaluation.
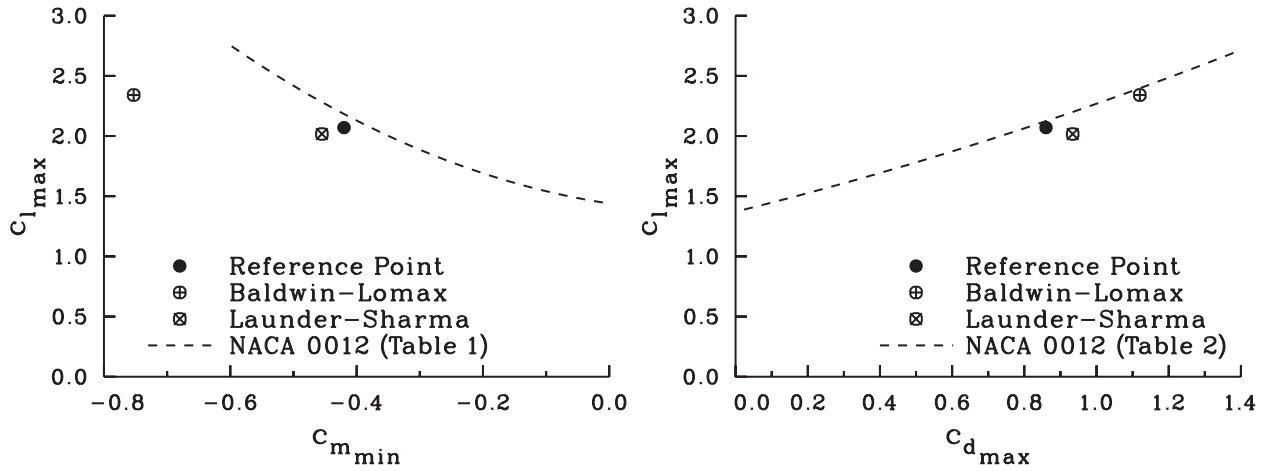
Figure 20. Comparison of Navier-Stokes predictions for NACA 0012 airfoil data using two turbulence models (Ref. 26).
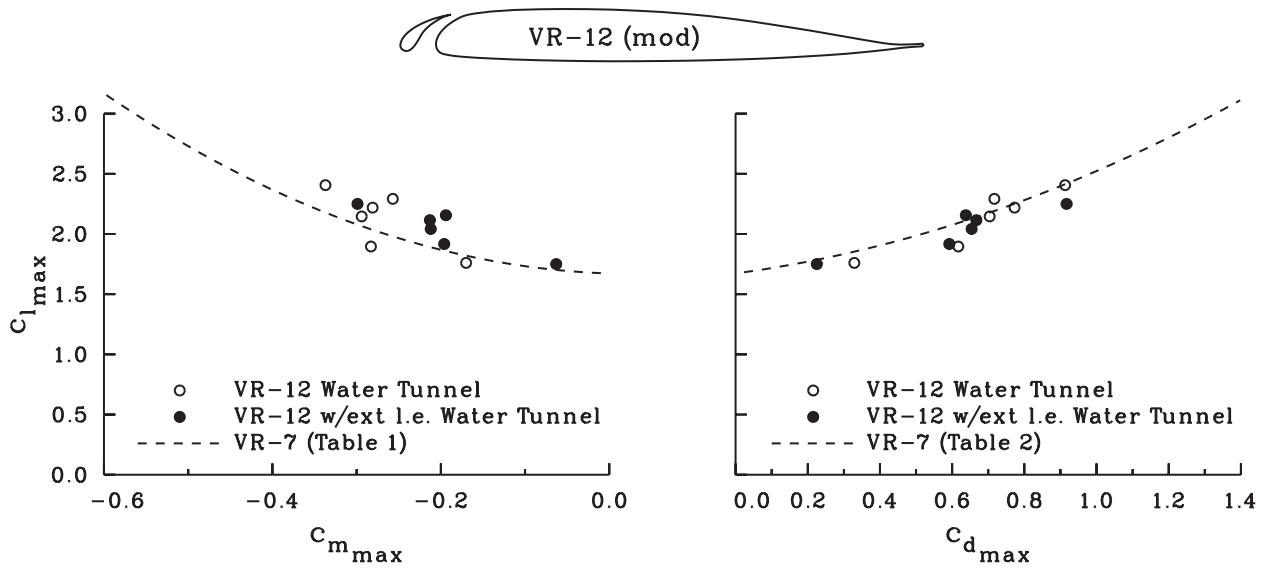

Figure 21. Comparison of dynamic stall extrema for a basic VR–12 with an extendable leading-edge slat (Ref. 27).

In Ref. 27, Plantin de Hugues et al. examined the dynamic stall performance of a VR–12 airfoil with and without an extendable leading edge slat. These data were obtained in the identical fashion as previously discussed for the VR–7 airfoil, Ref. 15. The extendable slat was designed, so that when retracted, the slat would fit inside the profile of the unmodified VR–12. The experimental data obtained in the water tunnel for both the basic VR–12 (slat retracted) and with the slat extended are shown in

Fig. 21. The airfoil profile with the slat extended is also illustrated. No dynamic stall data are available for the VR–12 from wind tunnel testing, so the polynomials for the VR–7 airfoil from Tables 1 and 2 are used as an approximate representation of the baseline airfoil's dynamic stall function. The water tunnel data for the VR–12 airfoil show generally good agreement with VR–7 polynomials based on the Ames tests. The effect of the extendable slat on the dynamic stall performance is negligible, as essentially
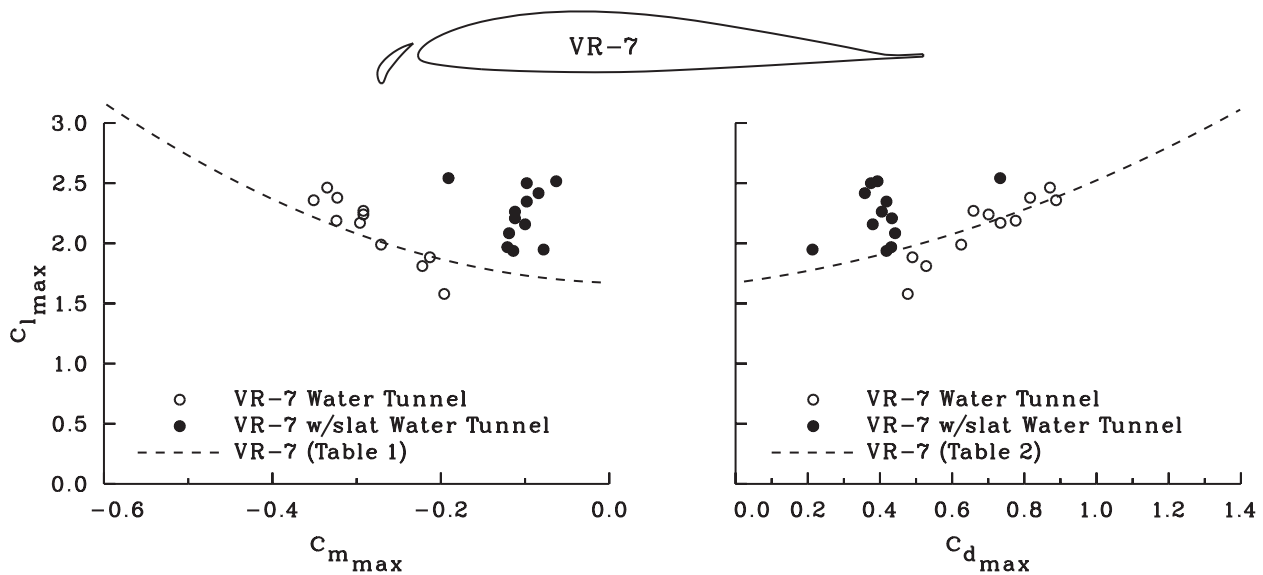
Figure 22. Comparison of dynamic stall extrema for a basic VR–7 airfoil and a VR–7 with a leading-edge slat (Ref. 15).

the same dynamic stall function is obtained with or without the leading-edge slat. For identical test conditions, the extendable slat appears to reduce the strength of the dynamic stall vortex, but this gives no advantage in dynamic stall performance over a conventional single-element airfoil.

A VR–7 airfoil was tested in the Ames water tunnel in a configuration with a leading edge slat (Ref. 15). The slat design was different from the VR–12 configuration just discussed. Baseline data for this configuration have already been shown in Fig. 9. The baseline data are repeated in Fig. 22, along with the data obtained with the slat. The VR–7 dynamic stall function, from Tables 1 and 2, are also included in the figure. As previously noted, the water tunnel data for the basic VR–7 airfoil show good agreement with the dynamic stall function based on the Ames wind tunnel tests. Unlike the VR–12 with an extendable leading edge, the dynamic stall performance of the VR–7 with the leading-edge slat is very different from the baseline airfoil. This multi-element configuration shows a substantially augmented lift capability with a reduced penalty in terms of pitching moment and drag. In this sense, this airfoil is clearly an improvement over a conventional single-element airfoil.

6   Design Considerations

The dynamic stall function provides a useful means of evaluating the experimental characteristics of conventional airfoils as well as of novel designs, as illustrated here for two multi-element airfoils. This comparison also points out that it is not sufficient to suppress the dynamic stall vortex or reduce its strength, if the only result is that the lift, moment, and drag are simply shifted to lower values. The reality of a maneuver on a helicopter is the necessity of achieving a maximum thrust capability. If a new design simply shifts the location on the dynamic stall function where dynamic stall occurs, this has no utility, as the pilot will persist in moving the flight controls until maximum thrust is achieved. A comparison, therefore, of a novel design with a current airfoil must be done on the basis of the moment and drag penalties that occur at a constant lift level. A comparison of two airfoils for the same α_0, α_1, and k values is not sufficient if the same lift is not obtained.

7   Concluding Remarks

The loading on an airfoil, measured during two-dimensional dynamic stall testing, was evaluated for eight airfoils tested in the NASA-Ames 7- by 10-Foot

38.19

Wind Tunnel by McCroskey and his colleagues and for a ninth airfoil tested subsequently by Piziali. The loading, characterized by the peak airfoil lift and drag, and minimum pitching moment, is shown to be similar over a wide range of test conditions. The loading characteristic is herein termed the dynamic stall function and is a useful measure of airfoil dynamic stall performance.

The dynamic stall function was characterized using 2nd-order polynomials for maximum lift as a function of minimum moment, and maximum lift as a function of maximum drag. The steady polynomial coefficients, a_0 and b_0, are shown to be closely related to the airfoil's static $c_{l_{max}}$. In general, the a_0 and b_0 values show an increment of 0.05 to 0.12 in lift over the static $c_{l_{max}}$. This indicates that an airfoil with an improved $c_{l_{max}}$ will also show improved dynamic stall performance.

The dynamic stall functions obtained from the Ames tests were compared to other dynamic stall data from a variety of test facilities and generally good agreement was obtained.

The dynamic stall function appears to be relatively insensitive to a number of operational parameters and this was particularly noted in the case of Reynolds number. Essentially identical results were obtained for a water tunnel test with a Reynolds number of 100,000 to 250,000 as for a wind tunnel test with a Reynolds number of 4 million. This insensitivity to Reynolds number is a clear indication of the dominating effect on the loading of the dynamic stall vortex.

The dynamic stall function measured in flight during a severe maneuver was examined and, although the scatter is greatly increased relative to two-dimensional tests in the wind tunnel, similar behavior is observed. An examination of the three-dimensional characteristics for the flight case was made. The dynamic stall vortex extends right to the tip with little reduction in the augmented lift. These three-dimensional effects are compared to dynamic stall on an oscillating wing (obtained in a wind tunnel) where the dynamic stall vortex disappears within a blade chord of the tip. Although both tests show some three-dimensional effects at the tip, these are weak for the flight aircraft and strong for the oscillating wing and, hence, the two test cases are poor analogues. However, the highly two-dimensional character of the flight data provides encouragement that an accurate prediction of three-dimensional effects is not important for the prediction of dynamic stall on a flight vehicle.

The dynamic stall function was used to evaluate the prediction of semi-empirical models, CFD methods, and experimental tests of multi-element airfoils. These comparisons have emphasized that in evaluating new or improved airfoils, merely suppressing the dynamic stall vortex has little utility. Rather, a new design should have lower moment and drag penalties for the same airfoil lift.

8   References

1. F. J. McHugh, "What Are the Lift and Propulsive Force Limits at High Speed for the Conventional Rotor?" American Helicopter Society 34th Annual National Forum, Washington, D.C., May 15-17, 1978.

2. F. J. McHugh, Ross Clark, and Mary Soloman, "Wind Tunnel Investigation of Rotor Lift and Propulsive Force at High Speeds–Data Analysis," NASA CR 145217-1, October 1977.

3. F. D. Harris, "Rotary Wing Aerodynamics–Historical Perspective and Important Issues," American Helicopter Society National Specialists' Meeting on Aerodynamics and Aeroacoustics, Arlington, TX, February 29-27, 1987.

4. F. J. Davenport and J. V. Front, "Airfoil Sections for Rotor Blades—A Reconsideration," American Helicopter Society 22nd Annual Forum, Washington, D.C., May 12, 1966.

5. J. L. McCloud III and George B. McCullough, "Wind-Tunnel Tests of a Full-Scale Helicopter Rotor with Symmetrical and with Cambered Blade Sections at Advance Ratios from 0.3 to 0.4," NASA TN 4367, September 1958.

6. W. J. McCroskey, "Some Current Research in Unsteady Fluid Dynamics–The 1976 Freeman Scholar Lecture," *Journal of Fluids Engineering*, Vol. 99, March 1977, pp. 8–38.

7. L. W. Carr, "Progress in Analysis and Prediction of Dynamic Stall," *Journal of Aircraft*, Vol. 25, No. 1, January 1988, pp. 6–17.

8. W. J. McCroskey, K. W. McAlister, L. W. Carr, and S. L. Pucci, "An Experimental Study of Dynamic Stall on Advanced Airfoil Sections Volume 1. Summary of Experiments," NASA TM 84245, July 1982.

9. K. W. McAlister, S. L. Pucci, W. J. McCroskey, and L. W. Carr, "An Experimental Study of Dynamic Stall on Advanced Airfoil Sections Volume 2. Pressure and Force Data," NASA TM 84245, September 1982.

10. L. W. Carr, W. J. McCroskey, K. W. McAlister, S. L. Pucci, and O. Lambert, "An Experimental Study of Dynamic Stall on Advanced Airfoil Sections Volume 3. Hot-Wire and Hot-Film Measurements," NASA TM 84245, December 1982.

11. W. G. Bousman, "Airfoil Dynamic Stall and Rotorcraft Maneuverability," NASA TM–2000–209601, USAAMCOM TR-00-A-008, July 2000.

12. R. A. Piziali, "2-D and 3-D Oscillating Wing Aerodynamics for a Range of Angles of Attack Including Stall," NASA TM 4532, USAATCOM TR 94-A-011, September 1994.

13. A. O. St. Hilaire, F. O. Carta, M. R. Fink, and W. D. Jepson, "The Influence of Sweep on the Aerodynamic Loading of an Oscillating NACA 0012 Airfoil. Volume I – Technical Report," NASA CR-3092, February, 1979.

14. J. Renaud and J. Coulomb, "2D Simulation of Unsteady Phenomena on a Rotor," Paper No. 10, Fourth European Rotorcraft and Powered Lift Forum, Stresa, Italy, September 13-15, 1978.

15. K. W. McAlister and C. Tung, "Suppression of Dynamic Stall with a Leading-Edge Slat on a VR–7 Airfoil," NASA TP 3357, March 1993.

16. S. T. Gangwani, "Prediction of Dynamic Stall and Unsteady Airloads for Rotor Blades," American Helicopter Society 37th Annual Forum Proceedings, New Orleans, LA, May 17-20, 1981, pp. 1–17.

17. L. U. Dadone, "Two-Dimensional Wind Tunnel Test of an Oscillating Rotor Airfoil, Volume I," NASA CR-2914, December 1977.

18. L. U. Dadone, "Two-Dimensional Wind Tunnel Test of an Oscillating Rotor Airfoil, Volume II," NASA CR-2915, December 1977.

19. W. G. Bousman, "A Qualitative Examination of Dynamic Stall from Flight Test Data," American Helicopter Society 53rd Annual Forum Proceedings, Virginia Beach, VA, April 29-May 1, 1997, pp. 368–387.

20. K. Nguyen and W. Johnson, "Evaluation of Dynamic Stall Models with UH–60A Airloads Flight Test Data," American Helicopter Society 54th Annual Forum Proceedings, Washington, D.C., May 20-22, 1998, pp. 576-587.

21. R. E. Gormont, "A Mathematical Model of Unsteady Aerodynamics and Radial Flow for Application to Helicopter Rotors," USAAVLABS TR 72-67, May 1973.

22. W. Johnson, "The Response and Airloading of Helicopter Rotor Blades Due to Dynamic Stall," ASRL TR 130-1, May 1970.

23. C. M. Tan and L. W. Carr, "The AFDD International Dynamic Stall Workshop on Correlation of Dynamic Stall Models with 3-D Dynamic Stall Data," NASA TM 110375, July 1996.

24. D. Petot, "Differential Equation Modeling of Dynamic Stall," *La Recherche Aérospatiale*, No. 1989-5.

25. V. K. Truong, "A 2-D Dynamic Stall Model Based on a Hopf Bifurcation," Nineteenth European Rotorcraft Forum, Cernobbio, Italy, September 14-16, 1993.

26. O. Rouzaud and A. Plop, "2D Unsteady Navier-Stokes Computations at ONERA for Prediction of Dynamic Stall," Paper AE02, 24th European Rotorcraft Forum, Marseilles, France, September 15-17, 1998.

27. P. Plantin De Hugues, K. W. McAlister, and C. Tung, "Effect of an Extendable Slat on the Stall Behavior of a VR-12 Airfoil," NASA TP 3407, September 1993.